1   **TITLE PAGE**

2   **Loss of the RNA helicase *Dhx15* impairs endothelial energy metabolism,**

3   **lymphatic drainage and tumor metastasis in mice**

4   Jordi Ribera[1], Irene Portolés[1], Bernat Córdoba[1], Juan Rodríguez-Vita[1,2], Gregori

5   Casals[1], Bernardino González de la Presa[1], Mariona Graupera[3], Guadalupe

6   Soria[4], Raúl Tudela[4], Anna Esteve-Codina[5], Guadalupe Espadas[6], Eduard

7   Sabidó[6], Wladimiro Jiménez[1,7], William C. Sessa[8], Manuel Morales-Ruiz[1,7,*]

8   [1]Biochemistry and Molecular Genetics Department, Hospital Clínic of

9   Barcelona, Institut d'Investigacions Biomèdiques August Pi i Sunyer (IDIBAPS),

10 Centro de Investigación Biomédica en Red de Enfermedades Hepáticas y

11 Digestivas (CIBERehd), Barcelona, Spain.

12 [2]German Cancer Research Center, Heidelberg, Germany.

13 [3]Vascular Signalling Laboratory, Program Against Cancer Therapeutic

14 Resistance (ProCURE), Institut d'Investigació Biomèdica de Bellvitge (IDIBELL).

15 CIBERonc, Barcelona, Spain.

16 [4]Experimental 7T-MRI Unit, IDIBAPS, Barcelona, Spain, CIBERbbn, University

17 of Barcelona, Barcelona, Spain tudela.mri@gmail.com, gsoriar@clinic.cat.

18 [5]CNAG-CRG, Centre for Genomic Regulation (CRG), Barcelona Institute of

19 Science and Technology (BIST), Universitat Pompeu Fabra (UPF), Barcelona,

20 Spain. (anna.esteve@cnag.crg.eu)

21 [6]Proteomics Unit, Centre for Genomic Regulation (CRG), The Barcelona

22 Institute for Science and Technology, Universitat Pompeu Fabra, Barcelona,

23 Spain.

24 [7]Department of Biomedicine-Biochemistry Unit, School of Medicine University of

25 Barcelona, Barcelona, Spain.

26   [8]Department of Pharmacology, Department of Cardiology, Vascular Biology and

27   Therapeutics Program, Yale University School of Medicine, New Haven,

28   Connecticut, USA.

29   * **Corresponging author:** Dr. Manuel Morales-Ruiz, Department of

30   Biochemistry and Molecular Genetics, Hospital Clinic of Barcelona, 170

31   Villarroel Street, 08036 Barcelona, Spain; e-mail: morales@clinic.ub.es

32

ABSTRACT

DHX15 is an ATP-dependent RNA helicase involved in pre-mRNA splicing and a downstream substrate for Akt1, which plays a significant role in vascular biology. The aim of this study was to explore the regulatory function of DHX15 over the vasculature and endothelial cell biology. **Results:** DHX15$^{-/-}$ was lethal in mouse and zebrafish embryos. DHX15$^{-/-}$ zebrafish also showed an undeveloped parachordal line, which leads to the formation of lymphatic structures. DHX15$^{+/-}$ mice triggered lower vascular network density and impaired lymphatic function postnatally. Transcriptome and proteome analysis of DHX15 silenced LEC revealed alterations in the glycolysis and gluconeogenesis pathways. The validation of these results demonstrated an uncoupling of the glycolysis with the oxidation of pyruvate in the mitochondria and a lower activity of the Complex I, resulting in lower cellular ATP production. Noteworthy, DHX15$^{+/-}$ mice partially inhibited primary tumor growth and reduced lung metastasis after injection of LLC1 tumor cells.

Keywords: DHX15, endothelial cell, metabolism, vascular biology, vascular function.

INTRODUCTION

59   RNA helicases are highly conserved and widespread enzymes that play a

60 fundamental role in RNA metabolism through the control of basic RNA

61 processes such as ribosome formation, pre-mRNA maturation, nuclear

62 transportation, RNA translation, transcription initiation, degradation and folding

63 of RNA (Patel and Donmez, 2006). They also play an essential role in the

64 detection of viral RNAs (Jankowsky et al., 2011). RNA helicases are classified

65 into two different subfamilies: the DEAD-box family (DDX), and the DEAH-box

66 (DHX) family (Jankowsky et al., 2011; Umate et al., 2011). Specifically, the DHX

67 family consists of 16 members, which have been identified based on their

68 homology within the amino acid sequences of the helicase domain (Suthar et

69 al., 2016; Umate et al., 2011).

70 RNA helicases act by remodelling RNA structures through ATP hydrolysis,

71 which exerts a mechanical force resulting in the alteration of the RNA

72 configuration that is fundamental for many cellular processes. This RNA

73 reconfiguration is due to the translocation of the helicase along the RNA which

74 unwinds RNA duplexes and dissociates bound proteins (Bourgeois et al., 2016;

75 Chen et al., 2001; Jankowsky et al., 2001). It has been recently discovered that

76 since DHX helicases lack target selectivity they require the action of adapter

77 proteins, such as G-patch proteins, to aid in the recruitment of RNA targets to

78 the functional site of the helicase. These kind of DHX activators stabilize a

79 functional conformation with high RNA affinity enhancing the catalytic activity of

80 the helicase (Studer et al., 2020).

81 In recent years, RNA helicases have gained notoriety due to their role in cell

82 maintenance, controlling many biological processes, including cell differentiation

4

83   and apoptosis (Jiang and Wu, 1999). Also, several groups have linked the

84   defects in helicase functioning with cancer, infectious diseases, and

85   neurodegenerative disorders (Jankowsky et al., 2011). For instance, recent

86   studies have shown that the deregulated expression of an increasing number of

87   these enzymes usually appears in many types of tumors (Abdelhaleem, 2004;

88   Robert and Pelletier, 2013), hence being related to carcinogenesis and cancer

89   progression (Abdelhaleem et al., 2003; Fuller-Pace, 2013, 2006; Heerma van

90   Voss et al., 2017; Steimer and Klostermeier, 2012). Despite these initial studies,

91   the understanding of the pathological mechanisms driven by the RNA helicases

92   and their individual specificity or redundancy over their molecular targets is still

93   limited.

94   DHX15 is a newly identified member of the DEAH-box RNA helicase family,

95   located in the cell nucleus that regulates pre-mRNA maturation (Fouraux et al.,

96   2002; Niu et al., 2012). DHX15 is known to contribute to ribosome biogenesis

97   by participating in some steps of the small subunit maturation, and in splicing by

98   dissociating the spliceosome modules after completion of its function (Arenas

99   and Abelson, 1997; Combs et al., 2006; Martin et al., 2002; Tsai et al., 2005).

100   DHX15 has ubiquitous variable expression in healthy tissues and organs

101   (Imamura et al., 1997). This helicase is also present in retinal endothelial cells

102   that line the arborizing microvasculature in the human retina (Bharadwaj et al.,

103   2013). In pathological situations, some studies have shown that DHX15

104   expression can be dysregulated due to exacerbated autoimmune response

105   (Mosallanejad et al., 2014; Wang et al., 2016) and different types of cancer

106   (Albrecht et al., 2004; Lin et al., 2009; Nakagawa et al., 2006; Pan et al., 2017).

5

107   The serine/threonine kinase Akt1 plays an essential role in vascular biology as

108   a central signaling node that coordinates major cellular processes (Chen et al.,

109   2008; Lee et al., 2014; Pauta et al., 2016). Its primary signaling function relays

110   on the fact that Akt1-dependent phosphorylation leads to the regulation of

111   critical mediators that control different cellular processes, including cell death,

112   cell growth, and chemotaxis. In a previous study, we demonstrated that only the

113   Akt1 isoform can phosphorylate DHX15 in mouse lung endothelial cells (Lee et

114   al., 2014). This observation led us to hypothesize that DHX15 contributes to

115   some extent to the vascular functions of Akt. Therefore, the goal of the present

116   study was to characterize the vascular phenotypes and the pathological

117   mechanism associated with the DHX15 gene deficiency generated by gene

118   editing of this enzyme in mice and zebrafish.

119

120

121

122

123

124

125

126

127

128

129

130

6

131   **RESULTS**

132   **Homozygous loss of DHX15 gene is associated with embryonic lethality in**

133   **mice.** The physiological and pathophysiological effect of perturbations in the

134   DHX15 gene has not previously been assessed due to the lack of genetically

135   modified experimental models for this gene. Therefore, we generated a global

136   knockout mouse for DHX15 as described under the Materials and Methods

137   section. Exon 2 of the *DHX15* gene was selected as TALEN target site for

138   knockout mouse production, resulting in two different DHX15-deficient mouse

139   clones: Mouse-ID#35, and Mouse-ID#39. Both clones were used

140   interchangeably in the subsequent experiments without detecting significant

141   differences in the phenotypes or the results obtained (Fig. 1A).

142   Heterozygous DHX15 (DHX15$^{+/-}$) mice were viable without any apparent

143   phenotypic abnormalities but intercrosses between DHX15$^{+/-}$ showed no viable

144   homozygous mice (DHX15$^{-/-}$). To establish the embryonic lethality period, timed

145   pregnancies of DHX15$^{+/-}$ breeding were examined at embryonic day (E) 8.5. No

146   DHX15$^{-/-}$ embryos were obtained at this time point suggesting post-implantation

147   embryonic lethality before E8.5 (Fig. 1B).

148   **DHX15 gene deficiency causes blood and lymphatic vascular defects**

149   **during embryonic stages.** Previous studies demonstrated the role of Akt in

150   vascular development (Chen et al., 2008; Lee et al., 2014). To investigate

151   whether DHX15, as a downstream target of Akt, contributes to these vascular

152   defects we performed whole-mount blood vessel staining followed by 3D

153   visualization in E10.5 mouse embryos to quantify potential vascular

154   abnormalities. DHX15$^{+/-}$ embryos do not exhibit significant defects in

155   segmentation. However, heterozygous embryos showed lower vascular density

156   compared with wild-type (Fig. 1C). This deficiency is mainly evident in the heart

157   region and the intersomitic arteries that sprout out or are located between the

158   somites.

159   Early embryonic lethality caused in mice by DHX15 deficiency limits the

160   characterization of embryonic vascular anomalies motivated by this genetic

161   disturbance in homozygosis. In order to overcome this limitation, we generated

162   a DHX15 gene deficient zebrafish mutant by Crispr/Cas9 editing in a

163   Tg(*flk1*:EGFP) background, as described in the material and methods section.

164   Wild-type zebrafish embryos showed DHX15 mRNA expressed broadly across

165   the larvae on 5 day post fertilization (dpf) (Fig. 1D, panels a, d and g) with an

166   enriched expression in the vascular system, specifically in the dorsal aorta and

167   the intersegmental vessels (Fig. 1D panels c, f and i), as post-natal

168   development progresses (24, 48 and 72 hours). DHX15$^{-/-}$ zebrafish embryos at

169   the stage 5 dpf were also screened for the expression of GFP in the

170   vasculature. DHX15 deficiency caused vascular development impairment in

171   primary arteries and veins, compared with the wild-type embryos. This

172   impairment was characterized by generalized dilatation of the vasculature,

173   especially in the cardinal vein and the intersegmental vessels (ISV) (Fig 2A).

174   These defects were extended to developing lymphatic structures, such as the

175   parachordal line (Jung et al., 2017). In control embryos, the parachordal line

176   was detected in nearly every somite segment (Figure 3A, arrows). By contrast,

177   the number of parachordal lines was 63% lower in the DHX15$^{-/-}$ embryos.

178   Similar to mice, completed DHX15 deficiency was lethal in zebrafish. To

179   establish the embryonic lethality period, we monitored the larvae mortality

180   during the first 10 dpf (Fig. 2B). The DHX15$^{-/-}$ larvae started to die at 6 dpf and

8

181   reached a 100% mortality at the stage 8 dpf. These animals developed

182   morphological defects including encephalic and cardiac edema, scoliosis, and

183   impaired neural/eye growth; compared to wild-type embryos (Fig. 2C) and the

184   onset of these morphological defects was at 3 dpf. In contrast, DHX15$^{+/+}$ and

185   DHX15$^{+/-}$ did not show significant differences in survival throughout embryonic

186   development or postnatally.

187   **Vascular density and lymphatic functionality are impaired postnatally in**

188   **DHX15$^{+/-}$ mice.** Due to the mortality associated with the lack of DHX15 in

189   homozygotes, it was only possible to characterize the vascular role of DHX15 in

190   viable adult heterozygotic mice (DHX15$^{+/-}$). DHX15$^{+/-}$ mice showed significant

191   vascular malformations compared with wild-type mice. Whole-mount preparations

192   of trachea tissue for the quantification of vessel pruning demonstrated that

193   DHX15$^{+/-}$ mice exhibited reduced vascular densities and an impaired

194   connectivity between large vessels (arrows), compared with littermate WT mice

195   (Fig. 3A).

196   We also evaluated lymphatic function in adult DHX15$^{+/-}$ mice by two different

197   methodologies. First, fluorescent lymphangiographies were performed in

198   peripheral regions using FITC-dextran. The lymphatic vasculature of DHX15$^{+/-}$

199   mice depicted diminished fluid drainage, compared with WT mice in three different

200   peripheral tissues: the ear, the tail and the foodpad (Fig. 3B). Second, we

201   quantified lymphatic drainage of the contrast agent gadolinium in the hindlimbs

202   after femoral artery ligation. This model is associated with increased vascular

203   permeability and the consequent accumulation of fluid in interstitial spaces. For

204   this purpose, we performed MRI in WT and DHX15$^{+/-}$ mice, 4 weeks after the

205   femoral artery ligation. In the ischemic legs (red circles Fig. 3C), all the DHX15$^{+/-}$

206 mice showed impaired lymphatic drainage with the consequent significant

207 increase in gadolinium accumulation, as observed by the increase area under the

208 concentration curve calculated in DHX15$^{+/-}$ mice, compared to control animals

209 (57.72±3.19 vs. 44.45±2.35 nM·s, respectively; $p<0.05$).

210 **Mechanistic insights of DHX15 deficiency in mouse endothelial cells. Role**

211 **of DHX15 in carbohydrate metabolism.** The *in vivo* experiments documented

212 that reduced levels of DHX15 caused cardiovascular and lymphatic

213 abnormalities. To obtain information on the mechanisms responsible for these

214 phenotypes in both vascular systems, we performed RNAseq and proteomics in

215 endothelial cells with or without DHX15 gene silencing using a LEC cell line

216 engineered to express the Tet-On® induction system for silencing DHX15 (siL-

217 DHX15-LEC, see material and methods). The advantage of using this cell line is

218 that these cells maintain both cardiovascular and lymphatic endothelial cell

219 characteristics, enabling the potential extrapolation of the mechanistic findings

220 into both vascular systems (supplemental figure 1). For instance, LEC displayed

221 endothelial cell markers (CD31, eNOS and uptake of oxidized low-density

222 lipoprotein; supplemental figure 1A and C) but also classical lymphatic cell

223 markers (LYVE-1 and podoplanin; supplemental figure 1B and C, respectively).

224 Supplemental figure 1D documents the total DHX15 levels in the starting cells

225 with or without DHX15 silencing that were used for genomic and proteo-

226 genomics experiments. The RNA-seq experiment allowed us generating

227 122.968 paired-end reads that were successfully mapped to the mouse

228 reference GRCm38 genome assembly. After quality control analysis, four

229 samples per experimental condition were included in the analysis. A total of

230 5,408 isoforms were differentially expressed when considering a

10

231   stringent threshold of FDR < 0.001 (Supplementary Table S1). For the

232   proteomics experiment, protein extracts (n=5 for each experimental condition)

233   were digested into peptides and they were quantified by mass spectrometry

234   analysis, as described in material and methods. We prioritized those protein

235   variations that showed a p-value lower than 0.05 or when the protein was

236   present in one condition, and undetectable in all the cases of the other

237   experimental condition. The list of proteins with relevant changes in their

238   abundance due to the silencing of DHX15 are detailed in Supplementary Table

239   S2.

240   In an effort to understand the biological relevance of the -omis results, we

241   combined the results of the RNAseq and proteomic experiments and subjected

242   the final list to pathway analysis using the Ingenuity Pathway Analysis (IPA;

243   Ingenuity) database. The results were compared against global molecular

244   networks to identify associated diseases and canonical pathways affected by

245   the perturbation of DHX15. The DHX15 silencing significantly affects two

246   networks: 1) endocrine system disorders, organismal injury and abnormalities

247   and cancer, and 2) gastrointestinal disease, organismal injury and abnormalities

248   and carbohydrate metabolism (Supplemental figure 2, A and B). Also, the

249   reduction of DHX15, was associated with differential expression in nine

250   additional signalling pathways (Supplemental figure 3A). Among them, the

251   glycolysis and gluconeogenesis pathways.

252   To functionally validate these bioinformatic results, we measured the glycolytic

253   activity and ATP generation in LEC cells. In accordance to our findings, siL-

254   DHX15-LEC cells showed higher levels of glycolytic activity (measured as nM of

255   L-Lactate) compared to cells with the DHX15 wild-type gene (0.41±0.04 vs.

256 0.19±0.05 nM L-lactate, respectively; *p*<0.05) (Fig. 4A). The alterations in

257 glucose metabolism was linked to lower ATP production compared to WT LEC

258 cells (417.7±31.37 vs. 524.2±20.40 nM ATP, respectively; *p*<0.05) (Fig. 4B),

259 suggesting uncoupling between glycolysis and oxidative phosphorylation. In this

260 context, the rMATS analysis of alternative 5' splice site from the RNAseq data

261 identified 220 significant splicing event modifications (with FDR<5%, absolute

262 difference >5% and >70 number of reads) caused by DHX15 silencing

263 (Supplementary Table S3). Among these genes, NADH ubiquinone

264 oxidoreductase core subunit S1 (NDUFS1) showed a differential alternative

265 splicing characterized by the presence of an alternative 5' splice site, giving rise

266 to a longer exon 1 for NDUFS1, when DHX15 was silenced in LECs (Fig.4C).

267 This gene encodes a subunit of the mitochondrial respiratory chain complex I. In

268 agreement with this observation, the in-gel activity measurement of complex I

269 was reduced significantly by ~50% in the siL-DHX15-LEC condition, compared

270 with non-silenced LEC cells (0.50±0.04 vs. 1.00±0.03 relative units,

271 respectively; *p*<0.01) (Fig. 4D).

272 Next, to assess the impact of reduced energy biosynthesis in siL-DHX15-LEC,

273 we quantified cell proliferation and migration. Silencing of *DHX15* reduced BrdU

274 uptake compared to control LEC (55.53±0.49 vs. 66.43±0.46 % of cells BrdU

275 positives, respectively; *p*<0.01) (Fig. 5A). Accordingly, the reduction of DHX15

276 resulted in an impaired cell migration. Silenced DHX15-LECs presented

277 delayed wound-healing after 24 hours compared with control LEC, as measured

278 in a scratch-induced directional wound-healing assay (Fig. 5B).

279 **Heterozygous *DHX15* gene deficiency reduced tumor growth and**

280 **metastases**. Abnormal function of blood and lymphatic vessels plays a

281   pathological role in multiple pathological conditions including inflammation and

282   cancer. Also, there is a strong link between the lymphatic vasculature and tumor

283   spread, as lymphatic vessels constitute one of the main routes of metastasis in

284   most cancers (Achen and Stacker, 2008; Mumprecht and Detmar, 2009;

285   Sleeman and Thiele, 2009). Considering also that one of the pathways modified

286   by the reduction of DHX15 was "endocrine system disorders, organismal injury

287   and abnormalities and cancer", we aimed at evaluating the role of DHX15 in

288   tumor development.

289   First, we explored how the loss of DHX15 affected growth of tumors implanted

290   into WT and DHX15$^{+/-}$ mice by injecting syngeneic LLC1 cells (1×10^5) into the

291   flanks of both strains. We measured the volume of the primary tumors

292   implanted in these mice 21 days post-injection of the LLC1 cells. Primary

293   tumors were significantly smaller in DHX15$^{+/-}$ mice compared with controls

294   (0.54 ± 0.07 vs. 1.06 ± 0.17 cm^3, respectively; $p<0.01$) (Fig. 6, panels a and d).

295   Tumors from DHX15$^{+/-}$ mice also showed an impaired vascular network

296   characterized by smaller vascular perimeter, compared with WT littermates

297   (199.1 ± 9.81 vs. 312.5 ± 17.16 µm perimeter, respectively; $p<0.01$) (Fig. 6, panels

298   b and e). Since growth of the primary tumor is rate-limiting and precludes

299   analyses of metastasis in this model, we established a postsurgical metastasis

300   model. Three weeks after subcutaneous LLC1 cells implantation, primary

301   tumors were completely resected and postsurgical lung metastasis were

302   evaluated 2 weeks later. Fewer primary tumors from DHX15$^{+/-}$ mice

303   metastasized the lungs compared with wild-type mice ($p<0.01$) (Supplemental

304   figure 3B). Noteworthy, and considering the mice with lung metastasis, the

305   overall area of metastases was strongly decreased in DHX15$^{+/-}$ mice, compared

13

306   with the wild-type group (0.88±0.32 vs. 2.53±0.69 % lung metastases,

307   respectively; *p*<0.05) (Fig. 6, panels c and f).

308   To investigate further whether the differences in the size of lung metastasis

309   were due to a potential lower LLC1 cell sedding in the primary tumors, we

310   followed over time a group of mice with similar primary large-size tumors. In this

311   experimental group (size of primary tumors ranging from 0.81 to 1.13 cm^3), we

312   also found significant differences when we compared the areas of lung

313   metastasis between wild-type and DHX15$^{+/-}$ mice, being significantly lower in

314   the DHX15$^{+/-}$ mice (6.27±1.12 vs. 0.20±0.20 vs. % lung metastases,

315   respectively; p<0.01) (Fig. 6, lower right graph).

316

317

318

319

320

321

322

323

324

325

326

327

328

329

330

14

DISCUSSION

331

332   In previous studies, we identified DHX15 as a downstream target of Akt1, which

333   has the greatest influence on vascular regulation compared with the other Akt

334   isoforms (Chen et al., 2008; Lee et al., 2014; Pauta et al., 2016). Considering

335   this observation, we hypothesized as a starting point for this study that DHX15

336   may also play a role in the vascular function. Here, we show that homozygous

337   DHX15 deficiency was associated with embryonic mortality in mice. To

338   determine when lethality occurred, timed pregnancies of DHX15$^{+/-}$ breeding

339   were studied at E8.5. We did not detect any DHX15$^{-/-}$ embryos at this time point,

340   suggesting early lethality post-implantation. On the other hand, the loss of just

341   one DHX15 allele resulted in impaired lymphatic drainage and decreased

342   vascular blood density. These results are in agreement with the reduced cell

343   proliferation and migration that we observed in LEC after silencing the

344   expression of DHX15. Why vasculature is affected by the partial loss of DHX15

345   in adult mice remains unclear if we only consider the results of this experimental

346   model. Under this experimental setting, we cannot discard the possibility that

347   adult mice developed these vascular defects because of accumulated damage

348   occurring during the postnatal stage in the DHX15 deficiency background.

349   However, and by studying the role of this RNA helicase in DHX15 gene-

350   deficient zebrafish, we showed that the DHX15-related vascular defects are

351   also occurring during development. In this experimental model, we found that

352   DHX15$^{-/-}$ larvae were not viable. Also, these unviable larvae presented blood

353   vascular alterations and reduced formation of developing lymphatic structures,

354   which were associated with cardiac and encephalic edema in the embryos.

15

355 Some unaddressed questions are whether each member of the RNA helicases

356 family has unique physiological functions and whether they are used

357 redundantly by the cell. The lethal phenotype of the DHX15$^{-/-}$ mouse and

358 zebrafish embryo supports the concept that RNA helicases may present unique

359 functions and specificity for molecular targets, likely in combination with adapter

360 proteins as demonstrated by Studer et al. (Studer et al., 2020).

361 Vascular growth and lymphangiogenesis are crucial in tumor growth and

362 metastasis (He et al., 2015; Nishida et al., 2006). Therefore, we assessed the

363 role played by DHX15 deficiency in tumor formation and expansion. After

364 performing syngeneic LLC1 cells allotransplantation in mice, we found that

365 heterozygous DHX15 deficiency partially inhibits primary tumor growth and

366 reduced lung metastases. This effect was associated with an intratumoral

367 reduction in the length of the blood vessel capillaries. Our results agree with

368 several clinical studies that underline a role of DHX15 in tumor progression in

369 several types of cancer, such as acute myeloid leukemia (Pan et al., 2017),

370 hepatocellular carcinoma (Xie et al., 2019), malignant peripheral nerve sheath

371 tumors (Nakagawa et al., 2006), prostate cancer (Jing et al., 2018) and non-

372 small-cell lung cancer (Yao et al., 2019). In all these situations, modifications of

373 DHX15 activity and/or its overexpression favors tumor growth. Several

374 mechanisms have been proposed in these studies to explain the tumorigenicity

375 effect of DHX15, such as the co-activation of the androgen receptor in prostate

376 cancer and the transcriptional activation of NF-kB in leukemia cells. In our

377 study, we provided an additional and a more general mechanism of DHX15 that

378 is relevant for tumor progression: the regulation of the growth and the function

379 of the vasculature.

16

380   The use of RNAseq and proteomics, combined with bioinformatics down-stream

381   analysis, is one of the most potent approaches to investigate the role played by

382   RNA helicases, as changes in differential splicing of a gene may or may not be

383   associated with changes in its protein abundance; therefore we need the

384   combined result of both high-throughput approaches. Adopting this strategy, we

385   were able to identify in the DHX15-silenced LEC significant changes in key

386   pathways that metabolize carbohydrates. Some of the genes products that

387   varied were UDP-glucose:glycoprotein glucosyltransferase 1, glyceraldehyde-3-

388   phosphate dehydrogenase, fructose-bisphosphate aldolase A, and pyruvate

389   kinase. This differential expression was also associated with a significant

390   increase in the lactate levels and a reduction in the intracellular concentration of

391   ATP. These metabolic changes suggest a regulatory compensatory effect of the

392   glycolytic enzymes due to the uncoupling of glycolysis with the oxidation of

393   pyruvate into the mitochondria. Supporting this possibility, we observed by

394   RNAseq significant expression changes in members of the family of the NADH

395   dehydrogenase [ubiquinone] 1 alpha subcomplex assembly factor (members

396   from NDUFS1, NDUFS5 and NDUFS7). These members are accessory

397   subunits of the mitochondrial membrane respiratory chain NADH

398   dehydrogenase (Complex I), that transfer electrons from NADH to ubiquinone in

399   the mitochondrial respiratory chain. Among them, we observed a significant

400   alteration in the splicing of the NDUFS1 gene. This alteration in gene splicing

401   was linked with a 50% reduction of the activity of the complex I in the

402   mitochondria of DHX15 silenced cells that may explain the decrease of ATP

403   intracellular levels and, as a consequence, the impairment in endothelial cell

404   proliferation and vascular growth.

17

405   Endothelial cells are mainly considered a glycolytic cell type that maintain their

406   energy demands by exploiting the glycolytic pathway preferentially without need

407   of coupling to the tricarboxilic acid cylce and the oxidative phosphorylation

408   (Martinive et al., 2006; Rath et al., 2012). However, some studies support the

409   notion that mitochondria electron transport chain activity is also playing a role in

410   driving endothelium angiogenesis and function. For example, low concentration

411   of oxygen results in the generation of mitochondrial ROS through the Complex

412   III of the electron transport chain (Bell et al., 2007). This increase in

413   mitochondrial ROS regulates angiogenic factors such as HIF-1a, promoting its

414   stabilization and allowing the transcription of the VEGFa gene (Jung et al.,

415   2013; Xia et al., 2007). Also, HUVEC and HDMEC depend on mitochondrial

416   oxidative phosphorylation to maintain energy supplies for proliferation and

417   growth, as demonstrated by measuring oxygen consumption and ATP

418   production in the presence of the mitochondrial uncoupler embelin (Coutelle et

419   al., 2014). Another transport electron chain inhibitor, rotenone that blocks

420   Complex I activity, reduced the angiogenic capacity of vasa vasorum

421   endothelial cells (Lapel et al., 2017). Our study is in line with these observations

422   and supports the idea that for optimal angiogenic response, endothelial cells

423   require dynamic crosstalk between glycolysis and mitochondria activity, driven

424   likely by regulators that promote a metabolic switch, as we have seen when we

425   modified the levels of DHX15.

426   In conclusion, our study establishes for the first time a vascular and metabolic

427   regulatory role for one RNA helicase member, DHX15, that has a repercussion

428   in pathological processes such as impaired lymphatic drainage and tumor

429   growth. Our results highlight the therapeutic potential of the modulation of

430   DHX15 expression in the context of these diseases. However, our study also

431   raised challenging and exciting questions concerning the function specificity and

432   the redundancy of the RNA-helicase family that need clarification before moving

433   forward in the selection of potential therapeutic targets from this family of

434   enzymes.

435

436

437

438

439 **MATERIALS AND METHODS**

440 ***DHX15 transgenic mice.*** *DHX15* gene deficient C57BL/6 mice were generated

441 by genomic editing by microinjecting TALEN (transcription activator-like effector

442 nuclease technology) RNA in pronucleated oocytes (Cyagen). The mouse

443 *DHX15* gene (GenBank accession number: NM_007839.3; Ensembl:

444 ENSMUSG00000029169) is located on chromosome 5. Fourteen exons have

445 been identified for this gene, with the ATG start codon in exon 1 and the TGA

446 stop codon in exon 14. Exon 2 was selected as TALEN target sites. TALENs

447 were constructed using the Golden Gate Assembly method (Cermak et al.,

448 2011) and confirmed by sequencing. The amplicons were then purified and sent

449 for DNA sequencing analysis. TALEN mRNAs generated by in vitro transcription

450 were injected into fertilized eggs for knockout mouse production (cDNA

451 sequence: TGTTGGTGAGACTGGGTC). The pups were genotyped by PCR

452 followed by sequence analysis. The positive founders were breeding to the next

453 generation, which was genotyped by PCR and DNA sequencing analysis. DNA

454 sequencing revealed two different DHX15-deficient mouse clones: Mouse-

455 ID#35 that was missing 8 bases in one strand, and Mouse-ID#39 that was

456 missing 1 base in one strand. Wild-type DNA was used as a negative control for

457 sequencing in parallel. The mRNA transcribed from targeted allele with

458 frameshift undergoes nonsense-mediated decay (NMD).

459 All animals were kept under constant temperature and humidity in a 12 hours

460 controlled dark/light cycle, and they were fed *ad libitum* on a standard pellet

461 diet. We performed the study following the guidelines of the Investigation and

462 Ethics Committees of the Hospital Clínic and the University of Barcelona.

20

463   ***Mouse genotyping.*** Mouse genomic DNA was isolated from tail biopsies using

464   a specific kit (Extract-N-Amp™ Tissue PCR Kit; Sigma-Aldrich, Darmstadt,

465   Germany). PCR was performed using the primer pairs to amplify the *DHX15*

466   gene (primer forward: 5′CACCAACCTGCCCCATACTCCT-3′ and primer

467   reverse: 5′-TGTATTGTCCCAGGGTAAAATGTGTTG-3′). PCR conditions were

468   as follows: 35 cycles at 94°C for 30 s, 59.3°C for 30 s, and 72°C for 60 s. PCR

469   product was sequenced by sanger sequencing to distinguish the *DHX15* wild

470   type mice and *DHX15* transgenic mice.

471   ***Immunological staining of mouse embryo whole-mounts.*** Embryos were

472   harvested at different points between E8.5 to E10.5. Embryos at E10.5 were

473   fixed in 4% paraformaldehyde overnight at 4ºC. For immunostaining of whole

474   mount embryos, after paraformaldehyde fixation, the embryos were sequentially

475   dehydrated in methanol and then incubated in the permeabilization buffer

476   (PBlec) (PBS pH6.8, 1% Tween 20, 1mM $CaCl_2$, 1mM $MgCl_2$, 0.1 mM $MnCl_2$)

477   for 20 minutes at room temperature. After permeabilization, the embryos were

478   incubated with primary antibody rat anti-endomucin (Abcam, Cambridge, UK)

479   (1:20 dilution) in PBlec buffer overnight at 4°C. To remove residual primary

480   antibody, embryos were washed with PBT (PBS pH6.8, 0.1% Tween) for 5×10

481   minutes. Next, the embryos were incubated with secondary antibody Alexa

482   Fluor 488-conjugated goat anti-rat (Thermo Fisher, Waltham, MA, USA) (1:500

483   dilution) in the dark overnight at 4ºC, and then washed with PBT for 3×10

484   minutes and postfix in 4% paraformaldehyde. Images were acquired using

485   fluorescence stereomicroscope (Leica Microsystems, Heerbrugg, Switzerland)

486   and immunofluorescence microscope (Nikon Eclipse E600, Kanagawa, Japan)

487   systems.

--

488   ***Generation of the Zebrafish animal model.*** Adults wild-type zebrafish (*Danio*

489   *rerio*), in a Tg(*flk1*:EGFP);Tg(*fabp10*:RFP) background, purchased from KIT -

490   European Zebrafish Resource Center (EZRC), were maintained at 28–29 °C on

491   a light cycle of 14 hours light/10 hours dark. The Crispr/cas9 design for gene

492   knock-out was performed as follows: Gene sequences were retrieved from

493   http://www.ncbi.nlm.nih.gov/gene   and

494   http://www.ensembl.org/Danio_rerio/Info/Index.   The sgRNA was designed

495   using the online tool http://crispor.tefor.net, based on exon site and high efficacy

496   and off-target published algorithms. Microinjection was performed at 1-cell

497   stage embryos. Fertilized zebrafish embryos were collected in E3 medium.

498   Then, embryos were grown at 28.5 °C.

499   ***Zebrafish whole mount in situ hybridization (ISH).*** cDNAs were amplified by

500   PCR from a custom zebrafish cDNAs library obtained by RT-PCR from an

501   mRNA pool coming from 5 days post fertilization zebrafish larvae. We included

502   a SP6 sequence linker in reverse primers to directly use the synthesized PCR

503   products as templates to amplify the reverse riboprobe to be used for ISH. For

504   the ISH, embryos were fixed overnight with 4% PFA and washed twice with

505   PBT. Then, embryos were incubated with hybridation buffer (50% formamide,

506   5X SSC buffer pH 6 (0.75M NaCl, 0.075M sodium citrate), 0.1% triton, 50

507   µg/mL yeast RNA, 50 µg/mL heparin) at least 1 hour. Next, embryos were

508   incubated with hybridation buffer containing the reverse riboprobe overnight.

509   Finally, embryos were washed with washing solution (50% formamide, 1X SSC

510   buffer, 0.1% Tween) 30 minutes twice and with MABT (100 mM maleic acid pH

511   7.5, 150 mM NaCl, 0.1% Tween) 10 minutes five times. Stained embryos were

512 processed for imaging with bright field stereoscope to determine the overall

513 expression pattern.

514 ***Zebrafish vascular characterization.*** Five-day old larvae obtained by pairwise

515 mating of adult Tg(*flk1*:EGFP;*fab10*:RFP; *DHX15*+/-) were sorted in two groups

516 depending on two criteria: a) curly larvae with abnormal development or b)

517 normal developed larvae. Larvae were flat-mounted and analyzed by confocal

518 imaging (Zeiss AxioObserver Z1) to evaluate putative phenotypical defects in

519 the trunk angiogenesis caused by the gene knockout. Genomic DNA extracted

520 from the whole embryos (using Extract-N-Amp™ Tissue PCR Kit, Sigma) was

521 used for the genotyping after vasculature imaging.

522 ***Mouse femoral artery ligation model and magnetic resonance imaging***

523 ***(MRI).*** Mice were anesthetized with a mixture of 4% isoflurane and 100%

524 oxygen. The femoral artery was isolated, and 5-0 suture was tied tightly around

525 artery at a ~3 mm distance to the inguinal ligament. Mice were allowed 4 weeks

526 to recover following the surgical procedure.

527 MRI experiments were conducted on a 7T BioSpec 70/30 horizontal animal

528 scanner (Bruker BioSpin, Ettlingen, Germany), equipped with a 12 cm inner

529 diameter actively shielded gradient system (400 mT/m) using a surface coil

530 dedicated to abdominal imaging. Animals were first anesthetized (1.5%

531 isoflurane in a mixture of 30% O_2 and 70% CO_2) and the tail vein was

532 cannulated for administration of contrast agent. Then, animals were transferred

533 under the same anesthesia regime to a Plexiglas holder in supine position with

534 a nose cone for administering anesthetic gases and fixed by a tooth bar, ear

535 bars and adhesive tape. 3D-localizer scans were used to ensure accurate

536 position of the animal's midline at the level of the posterior limbs in the isocenter

23

537 of the magnet. T2-weighted images were acquired by a RARE (rapid acquisition

538 with relaxation enhancement) sequence with an effective echo time (TE) of 24

539 ms, repetition time (TR) 1201 ms and RARE factor 8. Matrix size was 256x256

540 with an in-plane voxel size of 0.156x0.156 mm^2, 15 slices, slice thickness 1mm,

541 resulting in a field of view (FOV) of 40x40x15 mm^3. Time of flight 3D

542 angiography was acquired a FLASH (Fast Low Angle Shot) protocol with

543 TE=2.4 ms, TR=14000 ms, flip angle 20^0, 3 averages, matrix size:

544 448x256x128, voxel size 0.078x0.078x0.234 mm^3, resulting in a FOV of

545 35x20x30 mm^3. The shortening of the T1-relaxation time by the contrast agent

546 enhanced the tissue signal. T1 map was acquired using RARE-VTR (rapid

547 acquisition with relaxation enhancement and variable repetition time) sequence,

548 with TE=7 ms, 6 TR=200, 400, 800, 1500, 3000, 5500 ms, matrix size: 96x96x3,

549 voxel size 0.417x0.417x1 mm^3, resulting in a FOV of 40x40x3 mm^3.

550 To estimate the T1-relaxation rate and to measure the contrast agent relative

551 concentration DCE (dynamic contrast enhanced)-MR imaging was used with a

552 T1-weighted gradient-echo sequence. FLASH protocol was used with TE=1.5

553 ms, TR=12500 ms, flip angle 15^0, 600 repetitions and identical matrix, resolution

554 and FOV than T1 map. 0.025 mM/kg of gadoteridol was administered after the

555 first 100 repetitions were acquired as baseline. Altogether, the MRI session

556 lasted for 50 minutes approximately. After that, mice were returned to their

557 home cage under close supervision until they were recovered from the

558 anesthesia.

559 T1 maps were calculated in Paravision 6.0 software (Bruker BioSpin, Ettlingen,

560 Germany). Later these maps were processed with custom-made algorithms

561 programmed in Matlab (The MathWorks, Inc, Natick, MA, USA). A binary mask

562   was manually drawn over the T1 map in order to segment the muscle in both

563   legs. The first 40 volumes of the DCE acquistion were removed to assure the

564   signal stabilization. Also, the last 50 volumes were discarded to avoid second

565   pass effects. The slices of the temporal acquisition were spatially smoothed with

566   a Gaussian filter (standard deviation = 0.5) and temporal smoothed with a

567   moving average of 25 neighbors. The baseline of the signal was considered

568   using the 20 volumes after the 10th. The signal intensities of the temporal

569   acquisitions were converted to gadolinium concentrations using the method

570   described in (Barboriak et al., 2008; Li et al., 2000; Ortuño et al., 2013). The T1

571   map acquired before the DCE was used as reference values for the

572   magnetization and the Gadoteridol relaxivity was considered to be 3.35 $s^{-1}mM^{-1}$

573   (Shen et al., 2014). Finally, the obtained concentration curves were also

574   smoothed with a moving average of 9 neighbors. From the concentration

575   curves, different parameters were estimated, such as the time to peak (TTP),

576   the bolus arrival time (BAT) (using the method described in (Cheong et al.,

577   2003), relative time to peak (rTTP) (considering the bolus arrival time as starting

578   point), the wash in and wash out slopes, and the area under the gadolinium

579   concentration curve (AUC).

580   ***Mouse-induced tumor model.*** LLC1 (Mouse Lewis lung cancer cells) (ATCC,

581   Manassas, VA, USA) were cultured in Dulbecco's Modified Eagle Medium

582   (DMEM) supplemented with 10% fetal calf serum, 50 U/ml penicillin and 50

583   μg/ml streptomycin in humified atmosphere at 37°C and 5% CO_2. Syngeneic

584   LLC1 tumor cells ($1x10^5$) were subcutaneously injected into the flank of

585   DHX15$^{+/-}$ and wild-type mice. Primary tumor growth was controlled during the

586   first 3 weeks. Primary tumors were surgically removed 21 days after seeding.

587 Tumor volume was calculated by following formula: V = 4/3 x π x [length x

588 depth x width]. Primary tumors were fixed in 4% PFA and cryoconserved in

589 tissue-tek O.C.T. compound (Sakura, Flemingweg, Netherlands). The Post-

590 surgical metastasis model was performed as follows: Two weeks after primary

591 tumor removal, LLC1 injected mice showed distant metastasis formed in the

592 lungs. Tile scan images of haematoxylin-eosin (H&E) stained paraffin lung

593 sections were visualized using a microscope system (Nikon Eclipse E600,

594 Kanagawa, Japan) and the percentage of pulmonary metastatic area as percent

595 of total lung area was measured with Image J software (ImageJ version 1.52b;

596 National Institutes of Health, Bethesda, MD, USA).

597 ***DHX15 silencing in liver endothelial cells.*** The silencing of *DHX15* was

598 carried out in mouse primary hepatic endothelial cells immortalized with the

599 SV40 virus LEC; abmGood, Richmond, Canada), through shRNA by lentiviral

600 infection (Dharmacon, Lafayette, Colorado, USA). The SMARTvector

601 incorporated the bipartite 3G Tet-On® induction system, an inducible system

602 with minimal basal expression and potent activation after induction with

603 doxycycline. Cells were cultured in Microvascular Endothelial Cell Growth

604 Complete Medium (Pelobiotech, Planegg, Germany) in humified atmosphere at

605 37°C and 5% CO_2.

606 ***Proteome and transcriptome analysis of siL-DHX15-LECs.*** For proteomics,

607 proteins from non-silenced and DHX15-silenced LECs (1 mg/mL) were

608 extracted in 100 mM NH_4HCO_3, 8 M urea, 2.5 mM sodium pyrophosphate, 1

609 mM sodium orthovanadate and 1 mM β-glycerol phosphate buffer. Samples

610 were reduced with dithiothreitol (37 ºC, 60 min) and alkylated in the dark with

611 iodoacetamide (25 ºC, 30 min). The resulting protein extract was first diluted to

26

612   2M urea with 200 mM ammonium bicarbonate for digestion with endoproteinase

613   LysC (1:10 w:w, 37ºC, o/n, Wako, cat # 129-02541), and then diluted 2-fold with

614   200 mM ammonium bicarbonate for trypsin digestion (1:10 w:w, 37ºC, 8h,

615   Promega cat # V5113). After digestion, peptide mix was acidified with formic

616   acid and desalted with a MicroSpin C18 column (The Nest Group, Inc) prior to

617   LC-MS/MS analysis. Samples were analyzed using a LTQ-Orbitrap Fusion

618   Lumos mass spectrometer (Thermo Fisher Scientific, San Jose, CA, USA)

619   coupled to an EASY-nLC 1000 (Thermo Fisher Scientific (Proxeon), Odense,

620   Denmark). Peptides were loaded directly onto the analytical column and were

621   separated reversed-phase chromatography with a 90-min gradient (0-35%

622   ACN) in a 50-cm column with an inner diameter of 75 μm, packed with 2 μm

623   C18 particles spectrometer (Thermo Scientific, San Jose, CA, USA). Acquired

624   spectra were analyzed with ProteomeDiscoverer software (v2.0, Swiss-Prot

625   mouse database as in November 2016, 16831 entries). Protein abundances

626   were estimated with the average of the area corresponding to the three most

627   intense peptides. Protein abundance estimates were then log-transformed,

628   normalized by the median, and a fold change, and an adjusted *p-value* was

629   calculated with Perseus 1.5.6.0 (Supplementary Material). The raw proteomics

630   data have been deposited to the PRIDE repository with the dataset identifier

631   PXD018104.

632   The transcriptome analysis was carried out using RNAseq (HiSeq, Illumina).

633   Total RNA from *Mus musculus* was quantified by Qubit® RNA BR Assay kit

634   (Thermo Fisher Scientific) and the RNA integrity was estimated by using RNA

635   6000 Nano Bioanalyzer 2100 Assay (Agilent). The RNASeq libraries were

636   prepared with KAPA Stranded mRNA-Seq Illumina® Platforms Kit (Roche-Kapa

637 Biosystems) following the manufacturer´s recommendations. Briefly, 500ng of

638 total RNA was used as the input material, the poly-A fraction was enriched with

639 oligo-dT magnetic beads and the mRNA was fragmented. The strand specificity

640 was achieved during the second strand synthesis performed in the presence of

641 dUTP instead of dTTP. The blunt-ended double stranded cDNA was

642 3´adenylated and Illumina indexed adapters (Illumina) were ligated. The ligation

643 product was enriched with 15 PCR cycles and the final library was validated on

644 an Agilent 2100 Bioanalyzer with the DNA 7500 assay. The libraries were

645 sequenced on HiSeq 4000 (Illumina, Inc) in paired-end mode with a read length

646 of 2x76bp using HiSeq 4000 SBS kit in a fraction of a HiSeq 4000 PE Cluster kit

647 sequencing flow cell lane, following the manufacturer's protocol. Image

648 analysis, base calling and quality scoring of the run were processed using the

649 manufacturer's software Real Time Analysis (RTA 2.7.6) and followed by

650 generation of FASTQ sequence files by CASAVA. RNA-seq reads were

651 mapped against the mouse reference genome (GRCm38) using STAR version

652 2.5.2a (Dobin et al., 2013) with ENCODE parameters for long RNA. Genes

653 were quantified with RSEM version 1.2.28 (Li and Dewey, 2011) using the

654 gencode M12 version. Differential expression analysis was performed with

655 DESeq2 version 1.18 (Love et al., 2014) with default parameters. Differential

656 alternative splicing was performed with rMATS (Shen et al., 2014). Significant

657 splicing events with FDR<5%, absolute inclusion difference >5% and >70

658 number of reads were considered significant.

659 Signaling pathways altered by DHX15 deficiency were modeled using Ingenuity

660 Pathway Software (Ingenuity®Systems, Inc., Redwood City, USA). The

661 resulting *p-values* obtained by the Ingenuity Pathways Knowledge Base were

662 adjusted for multiple comparisons using Benjamini and Hochberg's method.

663 ***Separation of respiratory complexes and supercomplexes by Clear-Native***

664 ***Page (CN-PAGE) and in-gel activity of Complex I.*** Solubilization of

665 mitochondrial membranes by detergents, CN-PAGE, and staining was

666 performed as described by Jha et al. with minor modifications (Jha et al., 2017).

667 For this, after the mitochondria isolation from wild-type and siL-DHX15-LEC,

668 150µg of mitochondrial protein were suspended in a low-salt buffer (50 mM

669 NaCl, 50 mM imidazole, pH 7.0) and solubilized with digitonin (8 g/g protein, for

670 solubilization of respiratory chain supercomplexes). Immediately after the

671 electrophoretic run (4–13% gradient polyacrylamide gels), enzymatic

672 colorimetric reaction was performed. Complex I activity was determined by

673 incubating the gel with 2 mM Tris-HCl pH=7.4, 0.1 mg/mL NADH, and 2.5

674 mg/mL nitro blue tetrazolium (NTB) at room temperature. The original colour of

675 the complex I was preserved by fixing the gels in 50% methanol and 10% acetic

676 acid. After gel scanning, the intensity of each band was quantified by Image J

677 software (ImageJ version 1.52b; National Institutes of Health, Bethesda, MD,

678 USA).

679 ***Statistical analysis.*** In the case of homoscedasticity and normally distributed

680 data (assessed by Shapiro-Wilk test), groups were compared using a two-sided

681 Student t test or analysis of variance for independent samples. For other types

682 of data, Mann-Whitney U test, or Kruskal-Wallis test was used. Tukey's test

683 (with analysis of variance) or Dunn's test (with Kruskal-Wallis) was used as a

684 post hoc test to perform pairwise comparisons. The statistical analysis of

685 contingency tables for proportions was performed using the Fisher's exact test.

686   Differences were considered to be significant at a *p-value* less than 0.05. The

687   data are presented as the mean±standard error of the mean.

688

689

690

691

692

693

694

695

696

697

698

699

700

701

702

703

704

705

706

707

708

709

710   **ACKNOWLEDGEMENTS**

729

730 **CONFLICT OF INTEREST**

731 The authors do not have a conflict of interest.

732

733

734

735

31

REFERENCES

Abdelhaleem M. 2004. Over-expression of RNA helicases in cancer. *Anticancer Res* **24**:3951–3953.

Abdelhaleem M, Maltais L, Wain H. 2003. The human DDX and DHX gene families of putative RNA helicases. *Genomics* **81**:618–622. doi:10.1016/S0888-7543(03)00049-1

Achen MG, Stacker SA. 2008. Molecular control of lymphatic metastasis. *Ann N Y Acad Sci* **1131**:225–234. doi:10.1196/annals.1413.020

Albrecht B, Hausmann M, Zitzelsberger H, Stein H, Siewert JR, Hopt U, Langer R, Höfler H, Werner M, Walch A. 2004. Array-based comparative genomic hybridization for the detection of DNA sequence copy number changes in Barrett's adenocarcinoma. *J Pathol* **203**:780–788. doi:10.1002/path.1576

Arenas JE, Abelson JN. 1997. Prp43: An RNA helicase-like factor involved in spliceosome dissassembly. *Proc Natl Acad Sci U S A* **94**:11798–11802. doi:10.1073/pnas.94.22.11798

Barboriak DP, MacFall JR, Viglianti BL, Dewhirst MW. 2008. Comparison of Three Physiologically-Based Pharmacokinetic Models for the Prediction of Contrast Agent Distribution Measured by Dynamic MR Imaging. *J Magn Reson Imaging* **27**: 1388–1398.

Bell EL, Klimova TA, Eisenbart J, Moraes CT, Murphy MP, Budinger GRS, Chandel NS. 2007. The Qo site of the mitochondrial complex III is required for the transduction of hypoxic signaling via reactive oxygen species production. *J Cell Biol* **177**:1029–1036. doi:10.1083/jcb.200609074

Bharadwaj AS, Appukuttan B, Wilmarth PA. 2013. Role of the retinal vascular endothelial cell in ocular disease. *Prog Retin Eye Res* **32**: 102-180.

32

761   Bourgeois CF, Mortreux F, Auboeuf D. 2016. The multiple functions of RNA

762   helicases as drivers and regulators of gene expression. *Nat Rev Mol Cell*

763   *Biol* **17**:426–438. doi:10.1038/nrm.2016.50

764   Cermak T, Doyle EL, Christian M, Wang L, Zhang Y, Schmidt C, Baller JA,

765   Somia N V., Bogdanove AJ, Voytas DF. 2011. Efficient design and

766   assembly of custom TALEN and other TAL effector-based constructs for

767   DNA targeting. *Nucleic Acids Res* **39**:1–11. doi:10.1093/nar/gkr218

768   Chen J, Somanath PR, Razorenova O, Chen WS, Bornstein P, Byzova T V.

769   2008. Nihms-9148.Pdf **11**:1188–1196.

770   Chen JYF, Stands L, Staley JP, Jackups RR, Latus LJ, Chang TH. 2001.

771   Specific alterations of U1-C protein or U1 Small nuclear RNA can eliminate

772   the requirement of Prp28p, an essential DEAD Box splicing factor. *Mol Cell*

773   **7**:227–232. doi:10.1016/S1097-2765(01)00170-8

774   Cheong LH, Koh TS, Hou Z. 2003. An automatic approach for estimating bolus

775   arrival time in dynamic contrast MRI using piecewise continuous regression

776   models. *Phys Med Biol* **48**. doi:10.1088/0031-9155/48/5/403

777   Combs DJ, Nagel RJ, Ares M, Stevens SW. 2006. Prp43p Is a DEAH-Box

778   Spliceosome Disassembly Factor Essential for Ribosome Biogenesis. *Mol*

779   *Cell Biol* **26**:523–534. doi:10.1128/mcb.26.2.523-534.2006

780   Coutelle O, Hornig-Do HT, Witt A, Andree M, Schiffmann LM, Piekarek M,

781   Brinkmann K, Seeger JM, Liwschitz M, Miwa S, Hallek M, Krönke M,

782   Trifunovic A, Eming SA, Wiesner RJ, Hacker UT, Kashkar H. 2014.

783   Embelin inhibits endothelial mitochondrial respiration and impairs

784   neoangiogenesis during tumor growth and wound healing. *EMBO Mol Med*

785   **6**:624–639. doi:10.1002/emmm.201303016

786   Dobin A, Davis CA, Schlesinger F, Drenkow J, Zaleski C, Jha S, Batut P,

787   Chaisson M, Gingeras TR. 2013. STAR: Ultrafast universal RNA-seq

788   aligner. *Bioinformatics* **29**:15–21. doi:10.1093/bioinformatics/bts635

789   Fouraux MA, Kolkman MJM, Van Der Heijden A, De Jong AS, Van Venrooij WJ,

790   Pruijn GJM. 2002. The human La (SS-B) autoantigen interacts with

791   DDX15/hPrp43, a putative DEAH-box RNA helicase. *Rna* **8**:1428–1443.

792   doi:10.1017/S1355838202021076

793   Fuller-Pace F V. 2013. DEAD box RNA helicase functions in cancer. *RNA Biol*

794   **10**:121–132. doi:10.4161/rna.23312

795   Fuller-Pace F V. 2006. DExD/H box RNA helicases: Multifunctional proteins

796   with important roles in transcriptional regulation. *Nucleic Acids Res*

797   **34**:4206–4215. doi:10.1093/nar/gkl460

798   Heerma van Voss MR, van Diest PJ, Raman V. 2017. Targeting RNA helicases

799   in cancer: the translation trap. *Biochim Biophys Acta* **1898**: 510-520.

800   Imamura O, Sugawara M, Furuichi Y. 1997. Cloning and characterization of a

801   putative human RNA helicase gene of the DEAH-box protein family.

802   *Biochem Biophys Res Commun* **240**:335–340. doi:10.1006/bbrc.1997.7585

803   Jankowsky A, Guenther UP, Jankowsky E. 2011. The RNA helicase database.

804   *Nucleic Acids Res* **39**:338–341. doi:10.1093/nar/gkq1002

805   Jankowsky E, Gross CH, Shuman S, Pyle AM. 2001. Active disruption of an

806   RNA-protein interaction by a DExH/D RNA helicase. *Science (80-)*

807   **291**:121–125. doi:10.1126/science.291.5501.121

808   Jha P, Wang X, Auwerx J. 2017. Analysis of mitochondrial respiratory chain

809   supercomplexes using blue native polyacrylamide gel electrophoresis (BN-

810   PAGE). *Curr Protoc Mouse Biol* **6**: 1–14.

811 Jiang ZH, Wu JY. 1999. Alternative splicing and programmed cell death. *Proc*

812   *Soc Exp Biol Med* **220**:64–72. doi:10.3181/00379727-220-44346

813 Jing Y, Nguyen MM, Wang D, Pascal LE, Guo W, Xu Y, Ai J, Deng F, Masoodi

814   KZ, Yu X, Zhang J, Nelson JB, Xia S, Wang Z. 2018. Siah2-mediated

815   ubiquitination of androgen receptor **37**:638–650.

816   doi:10.1038/onc.2017.371.DHX15

817 Jung HJ, Kim Y, Chang J, Kang SW, Kim JH, Kwon HJ. 2013. Mitochondrial

818   UQCRB regulates VEGFR2 signaling in endothelial cells. *J Mol Med*

819   **91**:1117–1128. doi:10.1007/s00109-013-1049-6

820 Jung HM, Castranova D, Swift MR, Pham VN, Venero Galanternik M, Isogai S,

821   Butler MG, Mulligan TS, Weinstein BM. 2017. Development of the larval

822   lymphatic system in zebrafish. *Development* **144**:2070–2081.

823   doi:10.1242/dev.145755

824 Lapel M, Weston P, Strassheim D, Karoor V, Burns N, Lyubchenko T, Paucek

825   P, Stenmark KR, Gerasimovskaya E V. 2017. Glycolysis and oxidative

826   phosphorylation are essential for purinergic receptor-mediated angiogenic

827   responses in vasa vasorum endothelial cells. *Am J Physiol - Cell Physiol*

828   **312**:C56–C70. doi:10.1152/ajpcell.00250.2016

829 Lee MY, Luciano AK, Ackah E, Rodriguez-Vitad J, Bancroft TA, Eichmann A,

830   Simons M, Kyriakides TR, Morales-Ruiz M, Sessa WC. 2014. Endothelial

831   Akt1 mediates angiogenesis by phosphorylating multiple angiogenic

832   substrates. *Proc Natl Acad Sci U S A* **111**:12865–12870.

833   doi:10.1073/pnas.1408472111

834 Li B, Dewey CN. 2011. RSEM: accurate transcript quantification from RNA-Seq

835   data with or without a reference genome. *BMC Bioinformatics* **12**: 323.

35

836   Li KL, Zhu XP, Waterton J, Jackson A. 2000. Improved 3D quantitative mapping

837   of blood volume and endothelial permeability in brain tumors. *J Magn*

838   *Reson Imaging* **12**:347–357. doi:10.1002/1522-

839   2586(200008)12:2<347::AID-JMRI19>3.0.CO;2-7

840   Lin ML, Fukukawa C, Park JH, Naito K, Kijima K, Shimo A, Ajiro M, Nishidate T,

841   Nakamura Y, Katagiri T. 2009. Involvement of G-patch domain containing 2

842   overexpression in breast carcinogenesis. *Cancer Sci* **100**:1443–1450.

843   doi:10.1111/j.1349-7006.2009.01185.x

844   Love MI, Huber W, Anders S. 2014. Moderated estimation of fold change and

845   dispersion for RNA-seq data with DESeq2. *Genome Biol* **15**:1–21.

846   doi:10.1186/s13059-014-0550-8

847   Martin A, Schneider S, Schwer B. 2002. Prp43 is an essential RNA-dependent

848   ATPase required for release of lariat-intron from the spliceosome. *J Biol*

849   *Chem* **277**:17743–17750. doi:10.1074/jbc.M200762200

850   Martinive P, Defresne F, Bouzin C, Saliez J, Lair F, Grégoire V, Michiels C,

851   Dessy C, Feron O. 2006. Preconditioning of the tumor vasculature and

852   tumor cells by intermittent hypoxia: Implications for anticancer therapies.

853   *Cancer Res* **66**:11736–11744. doi:10.1158/0008-5472.CAN-06-2056

854   Mosallanejad K, Sekine Y, Ishikura-Kinoshita S, Kumagai K, Nagano T,

855   Matsuzawa A, Takeda K, Naguro I, Ichijo H. 2014. The DEAH-Box RNA

856   helicase DHX15 activates NF-κB and MAPK signaling downstream of

857   MAVS during antiviral responses. *Sci Signal* **7**:1–12.

858   doi:10.1126/scisignal.2004841

859   Mumprecht V, Detmar M. 2009. Lymphangiogenesis and cancer metastasis. *J*

860   *Cell Mol Med* **13**:1405–1416. doi:10.1111/j.1582-4934.2009.00834.x

861 Nakagawa Y, Yoshida A, Numoto K, Kunisada T, Wai D, Ohata N, Takeda K,

862   Kawai A, Ozaki T. 2006. Chromosomal imbalances in malignant peripheral

863   nerve sheath tumor detected by metaphase and microarray comparative

864   genomic hybridization. *Oncol Rep* **15**:297–303. doi:10.3892/or.15.2.297

865 Nishida N, Yano H, Nishida T, Kamura T, Kojiro M. 2006. Angiogenesis in

866   cancer. *Vasc Health Risk Manag* **2**:213–219.

867   doi:10.2147/vhrm.2006.2.3.213

868 Niu Z, Jin W, Zhang L, Li X. 2012. Tumor suppressor RBM5 directly interacts

869   with the DExD/H-box protein DHX15 and stimulates its helicase activity.

870   *FEBS Lett* **586**:977–983. doi:10.1016/j.febslet.2012.02.052

871 Ortuño JE, Ledesma-C, Arbayo MJ, Simões R V, Candiota AP, Arús C. 2013.

872   DCE@urLAB: a dynamic contrast-enhanced MRI pharmacokinetic analysis

873   tool for preclinical data. *BMC Bioinformatics* **14**.

874 Pan L, Li Y, Zhang HY, Zheng Y, Liu XL, Hu Z, Wang Y, Wang Jing, Cai YH, Liu

875   Q, Chen WL, Guo Y, Huang YM, Qian F, Jin L, Wang Jiucun, Wang SY.

876   2017. DHX15 is associated with poor prognosis in acute myeloid leukemia

877   (AML) and regulates cell apoptosis via the NF-kB signaling pathway.

878   *Oncotarget* **8**:89643–89654. doi:10.18632/oncotarget.20288

879 Patel SS, Donmez I. 2006. Mechanisms of helicases. *J Biol Chem* **281**:18265–

880   18268. doi:10.1074/jbc.R600008200

881 Pauta M, Rotllan N, Fernández-Hernando A, Langhi C, Ribera J, Lu M, Boix L,

882   Bruix J, Jimenez W, Suárez Y, Ford DA, Baldán A, Birnbaum MJ, Morales-

883   Ruiz M, Fernández-Hernando C. 2016. Akt-mediated foxo1 inhibition is

884   required for liver regeneration. *Hepatology* **63**:1660–1674.

885   doi:10.1002/hep.28286

886 Rath G, Saliez J, Behets G, Romero-Perez M, Leon-Gomez E, Bouzin C, Vriens

887   J, Nilius B, Feron O, Dessy C. 2012. Vascular hypoxic preconditioning

888   relies on TRPV4-dependent calcium influx and proper intercellular gap

889   junctions communication. *Arterioscler Thromb Vasc Biol* **32**:2241–2249.

890   doi:10.1161/ATVBAHA.112.252783

891 Robert F, Pelletier J. 2013. Perturbations of RNA helicases in cancer. *Wiley*

892   *Interdiscip Rev RNA* **4**:333–349. doi:10.1002/wrna.1163

893 Shen S, Park JW, Lu ZX, Lin L, Henry MD, Wu YN, Zhou Q, Xing Y. 2014.

894   rMATS: Robust and flexible detection of differential alternative splicing from

895   replicate RNA-Seq data. *Proc Natl Acad Sci U S A* **111**:E5593–E5601.

896   doi:10.1073/pnas.1419161111

897 Sleeman JP, Thiele W. 2009. Tumor metastasis and the lymphatic vasculature.

898   *Int J Cancer* **125**:2747–2756. doi:10.1002/ijc.24702

899 Steimer L, Klostermeier D. 2012. RNA helicases in infection and disease. *RNA*

900   *Biol* **9**:751–771. doi:10.4161/rna.20090

901 Studer MK, Ivanović L, Weber ME, Marti S, Jonas S. 2020. Structural basis for

902   DEAH-helicase activation by G-patch proteins. *Proc Natl Acad Sci*

903   201913880. doi:10.1073/pnas.1913880117

904 Suthar MK, Purva M, Maherchandani S, Kashyap SK. 2016. Identification and in

905   silico analysis of cattle DExH/D box RNA helicases. *Springerplus* **5**:1–13.

906   doi:10.1186/s40064-015-1640-0

907 Tsai RT, Fu RH, Yeh FL, Tseng CK, Lin YC, Huang YH, Cheng SC. 2005.

908   Spliceosome disassembly catalyzed by Prp43 and its associated

909   components Ntr1 and Ntr2. *Genes Dev* **19**:2991–3003.

910   doi:10.1101/gad.1377405

911   Umate P, Tuteja N, Tuteja R. 2011. Genome-wide comprehensive analysis of

912   human helicases. *Commun Integr Biol* **4**:118–137. doi:10.4161/cib.13844

913   Wang P, Zhu S, Yang L, Cui S, Pan W, Jackson R, Zheng Y, Rongvaux A, Sun

914   Q, Yang G, Gao S, Lin R, You F, Flavell R, Fikrig E, Haven N, Haven N,

915   Haven N, Chase C. 2016. HHS Public Access **350**:826–830.

916   doi:10.1126/science.aab3145.Nlrp6

917   Xia C, Meng Q, Liu LZ, Rojanasakul Y, Wang XR, Jiang BH. 2007. Reactive

918   oxygen species regulate angiogenesis and tumor growth through vascular

919   endothelial growth factor. *Cancer Res* **67**:10823–10830. doi:10.1158/0008-

920   5472.CAN-07-0783

921   Xie C, Liao H, Zhang C, Zhang S. 2019. Overexpression and clinical relevance

922   of the RNA helicase DHX15 in hepatocellular carcinoma. *Hum Pathol*

923   **84**:213–220. doi:10.1016/j.humpath.2018.10.006

924   Yao G, Chen K, Qin Y, Niu Y, Zhang X, Xu S, Zhang C, Feng M, Wang K. 2019.

925   Long Non-coding RNA JHDM1D-AS1 Interacts with DHX15 Protein to

926   Enhance Non-Small-Cell Lung Cancer Growth and Metastasis. *Mol Ther -*

927   *Nucleic Acids* **18**:831–840. doi:10.1016/j.omtn.2019.09.028

928

929

930

931

932

933

934

935

FIGURES AND LEGENDS
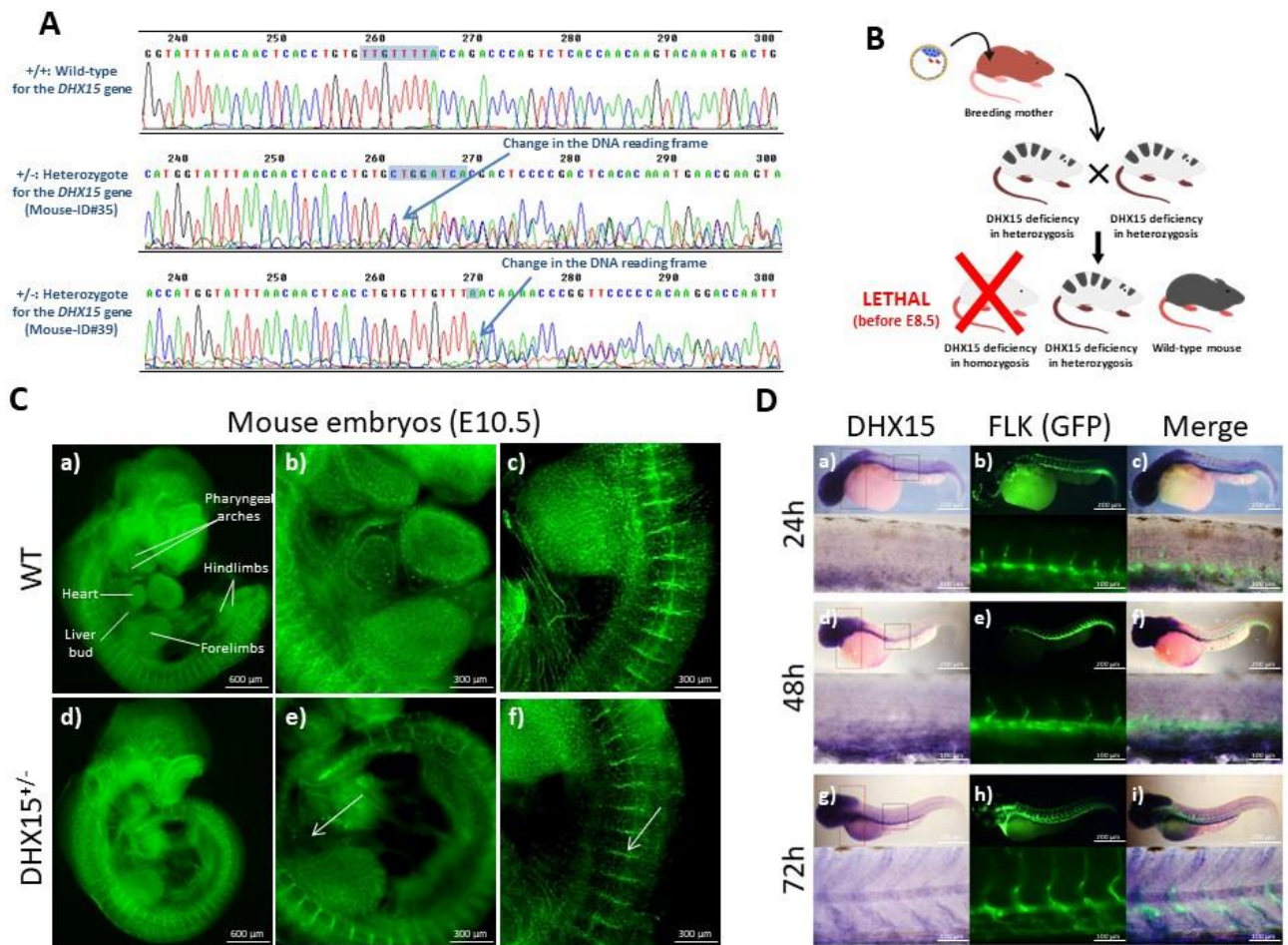
Figure 1. Embryonic characterization of DHX15 gene deficiency and expression in the gene-edited mouse and zebrafish models. (A) Comparison of sequencing chromatograms from wild-type and the heterozygote mouse of the *DHX15* gene obtained from the clones Mouse-ID#35 and Mouse-ID#39. The transcription activator-like effector nuclease technology (TALEN) target site is highlighted within the box. The arrow shows the first base from which the DNA reading frame undergoes nonsense-mediated decay. (B) Scheme showing the transgenic mouse production, from TALEN RNA injection in pronucleated oocytes. (C) Representative immunostaining of the vasculature with endomucin (green) from mouse embryos at the stage E10.5 of embryonic

40

948   development. The white arrows denote areas of decreased vascular density

949   (n=6). Maximal projection and 3D rendering from the microscope are showed

950   for each genotype. Original magnification: 20X and 40X. (D) Representative

951   results obtained from in situ hybridization using a labelled complementary RNA

952   strand to localize the specific DHX15 sequence on whole-mount zebrafish

953   embryos. DHX15 (blue) and vasculature (FLK1:EGFP; green) in zebrafish

954   embryos at 24, 48 and 72h of post-natal development. Merged panels show

955   DHX15 and vasculature (green) colocalization (n=15).

956

957

958

959

960

961

962

963

964

965

966

967

968

969

970

971

972

973
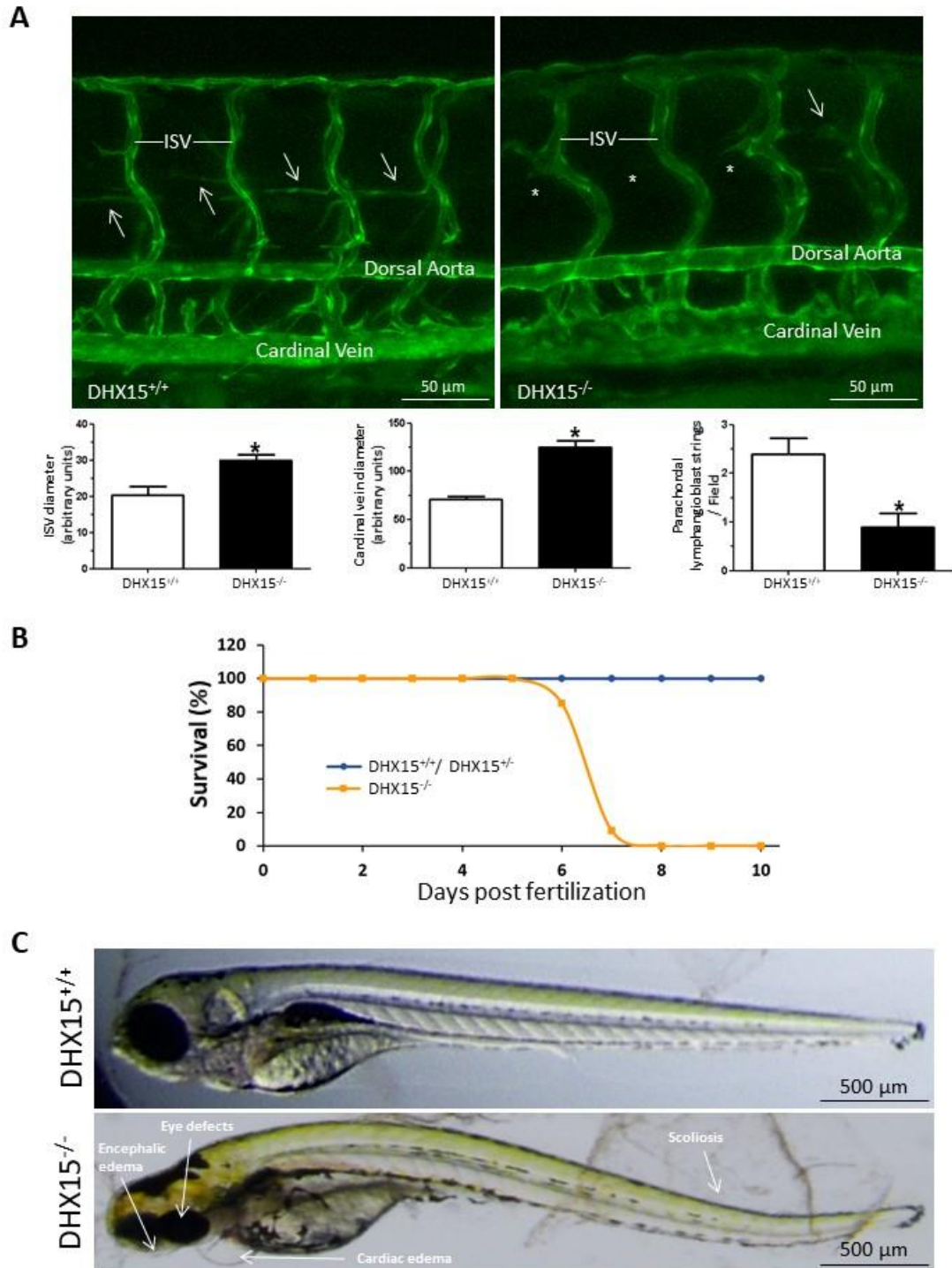
Figure 2. Characterization of embryonic vascular anomalies motivated by DHX15 gene deficient in zebrafish. (A) Representative vascular images of DHX15$^{+/+}$ and DHX15$^{-/-}$ larvae at 5 day post fertilization (dpf) revealing a reduced formation of the parachordal line (arrows). Asterisks denote the

42

978   absence of these vascular structures in DHX15$^{-/-}$ animals. Quantifications of

979   cardinal vein diameter, intersegmental vessels (ISV), and number of

980   parachordal structures are shown in the graphs; *p<0.01 vs. wild-type zebrafish.

981   (B) Survival assessment assay. The graph shows the larvae survival rate

982   through the first 10 dpf according to their different genotype (n=15). (C)

983   Representative images comparing wilt-type and DHX15$^{-/-}$ larvae at 7 dpf where

984   morphological defects including encephalic and cardiac edema, scoliosis, and

985   impaired neural/eye growth are evident.

986

987

988

989

990

991

992

993

994

995

996

997

998

999

1000

1001

1002
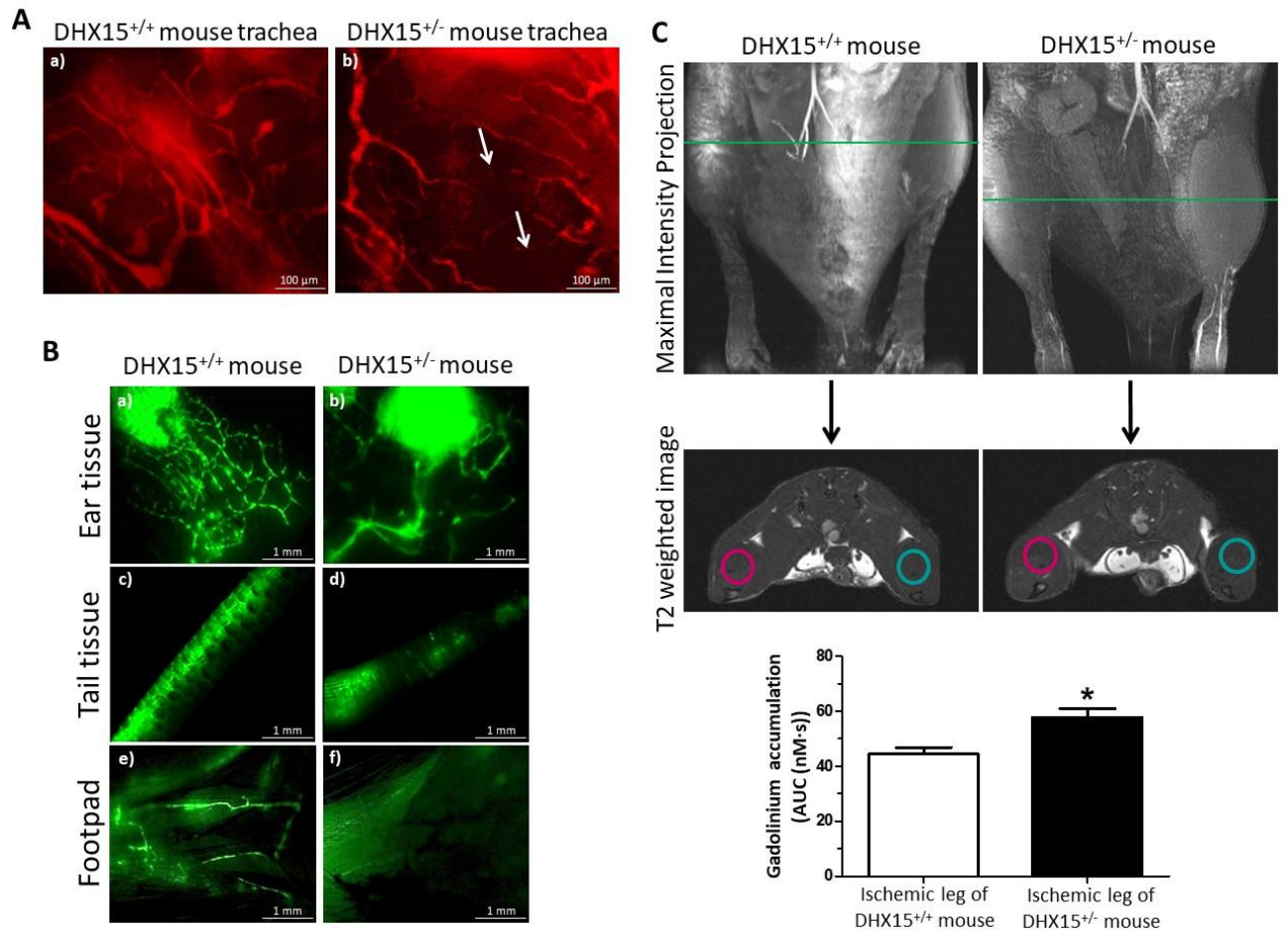
1003

Figure 3. DHX15$^{+/-}$ mice showed cardiovascular and lymphatic vasculature alterations. (A) Representative immunofluorescent images (red CD31 staining) of mouse trachea vessels. White arrowhead evidences lack of connectivity between large vessels (n=5). (B) Lymphatic drainage of 2000 KDa FITC-dextran analyzed by lymphangiography. Fluorescent dye was injected intradermally in the ear (panels a and b), in the interstitium of the tail-tip (panels c and d) and in the footpad (panels e and f) to assess lymphatic uptake (n=5). (C) Representative magnetic resonance images (MRI) for both strains of mice. First row shows the maximal intensity projection of the time of flight (TOF) angiography. The green line indicates the position of the coronal image (second row: T2 weighted image) where the regions of interest (ROIs) for the analysis of

44

1015 the dynamic contrast enhanced-MRI experiment where positioned. In blue,

1016 ROIs for the control leg, in red, ROIs for the ischemic leg. The lower graph

1017 shows the area under the concentration curve (AUC) calculated for the ischemic

1018 leg in WT and DHX15$^{+/-}$ mice; *p<0.05 vs. wild-type mouse (n=8).

1019

1020

1021

1022

1023

1024

1025
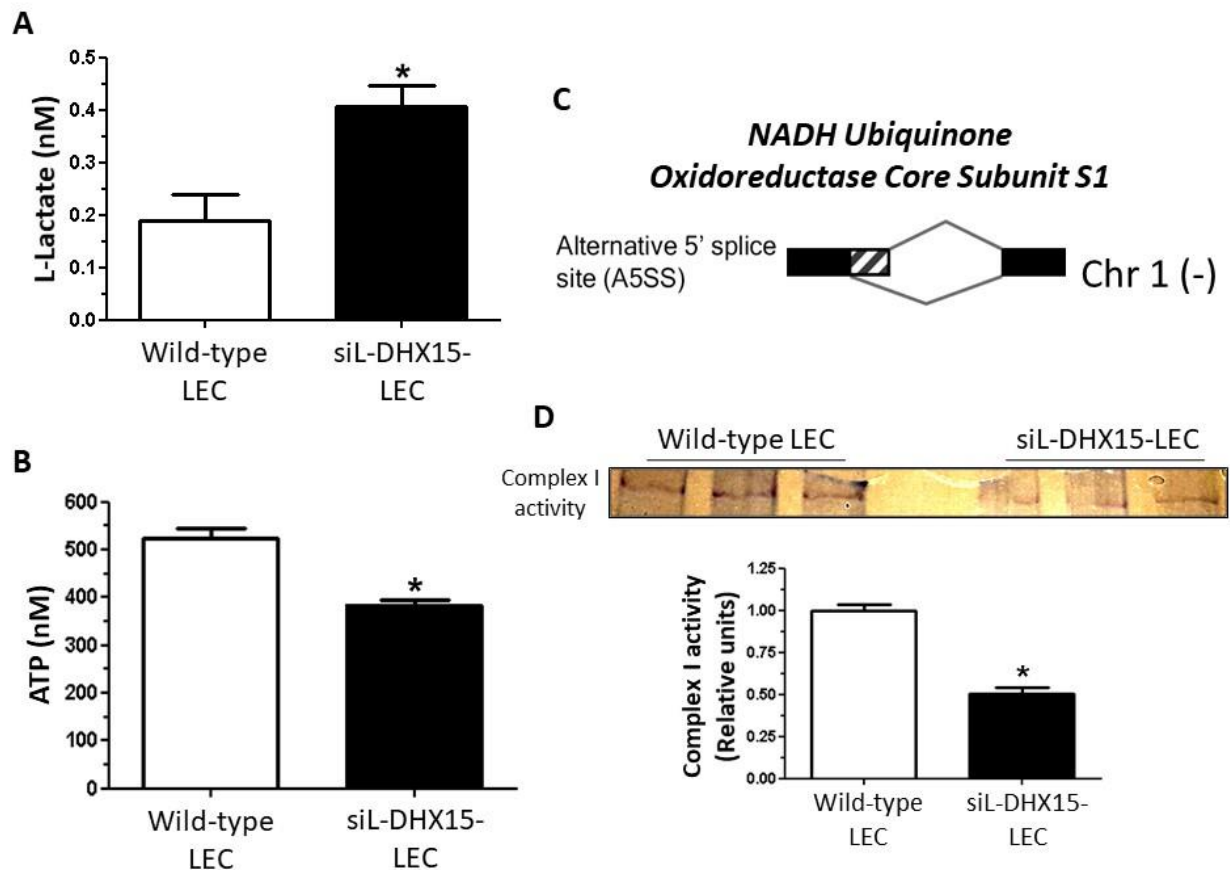
1026

1027

1028

1029

1030

1031

1032

1033

1034

1035

1036

1037

1038

1039

1040

Figure 4. Uncoupling of aerobic glucose metabolism in siL-DHX15-LEC.

(A) Glycolysis levels were evaluated by a colorimetric enzymatic reaction in wild-type and silenced DHX15 liver endothelial cells (siL-DHX15-LEC) as nM of L-Lactate; *$p<0.01$ *vs.* wild-type LEC (n=6). (B) ATP production was evaluated by a luminescence assay in wild-type and siL-DHX15-LEC; *$p<0.05$ *vs.* wild-type LEC (n=6). (C) Alternative splicing was quantified as described in Material and Methods. The diagram shows the significant splicing event occurring on the gene NDUFS1 with an inclusion level of 6% and a FDR=0.02. The striped bar represents the lengthening of the alternative 5' limit size of exon 1 caused by the DHX15 silencing. (D), *In-gel* activity staining on clear-native page (CN-PAGE) of the respiratory complex I from wild-type and siL-DHX15-LEC's

1052   mitochondria. The quantification of the relative band intensities of complex I

1053   activity is shown in the graph below; *$p<0.01$ vs. wild-type LEC (n=6).

1054

1055

1056

1057

1058

1059

1060

1061

1062
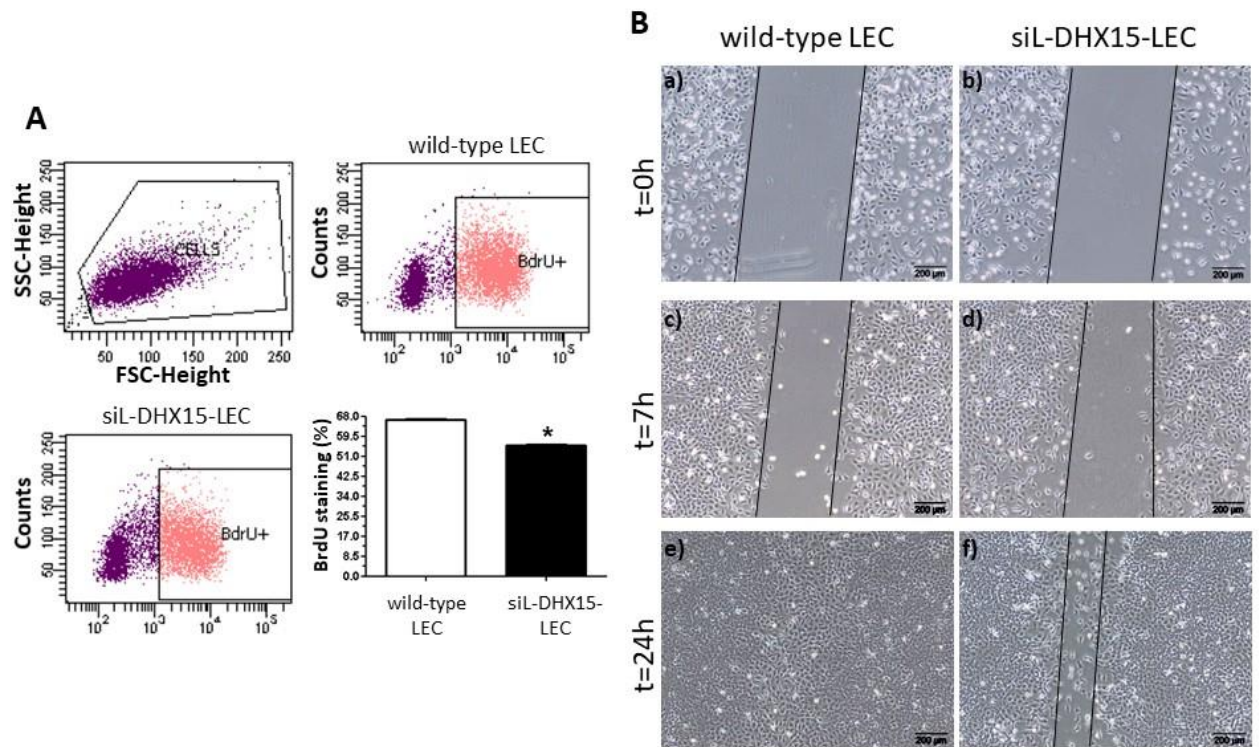
1063

1064

1065

1066

1067

1068

1069

1070

1071

1072

1073

1074

1075

1076

1077

Figure 5. siL-DHX15-LEC presented less cell migration and proliferation.

(A) Representative figures of the proliferation assay performed in wild-type and silenced DHX15 liver endothelial cells (siL-DHX15-LEC). Bromodeoxyuridine (BrdU) incorporation was quantified by flow cytometry. First panel shows a dot-blot graph of the cell population. Cells within the oval scatter gate were analyzed. The negative control population was chosen from cells cultured in the absence of BrdU. The percentage of cells that stained positively for BrdU for each experimental condition is depicted in the bar graph; *$p<0.01$ *vs.* wild-type LEC (n=6). (B) Cell migration was quantified after performing a scratch wound in confluent non-silenced and silenced LECs cells that were cultured in 6-well

1088   plates. Then images of wound healing were acquired after 0, 7 and 24 hours

1089   (n=6).

1090

1091

1092

1093

1094

1095

1096

1097

1098

1099
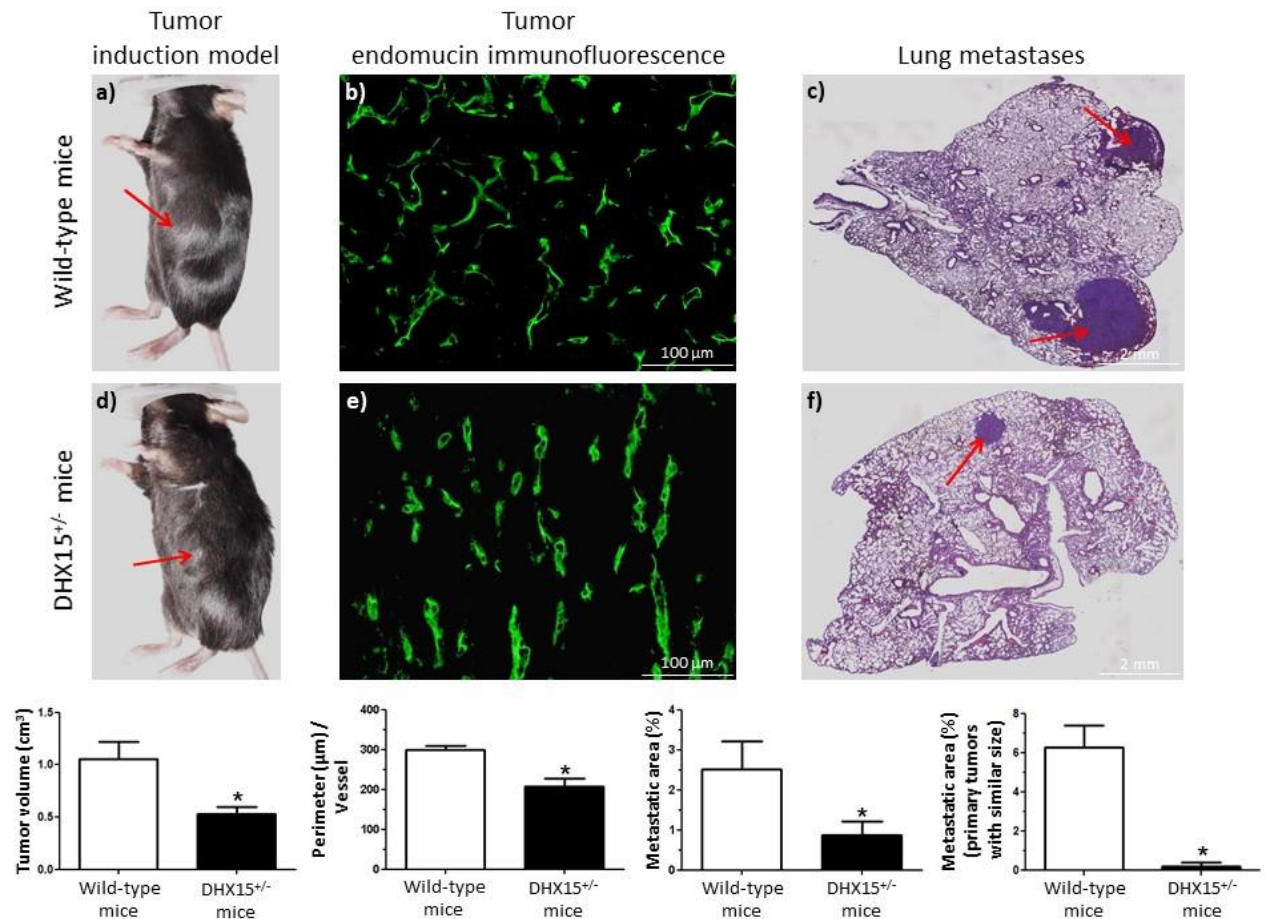
1100

1101

1102

1103

1104

1105

1106

1107

1108

1109

1110

1111

1112

1113

Figure 6. Tumor growth and metastases in DHX15$^{+/-}$ mouse. (A) Macroscopic images of tumor size in wild-type and DHX15$^{+/-}$ mice 3 weeks after mouse Lewis lung cancer cells (LLC1) implantation. The arrows indicate the primary tumor. The quantification of tumor volume (cm^3) is shown on the lower graph; *$p<0.01$ vs. wild-type mice (n=15). (B) Endomucin immunostaining of intratumoral blood vessels in wild-type and DHX15$^{+/-}$ mice. Quantification of vessel perimeter is shown in the graph below; *$p<0.01$ *vs.* wild-type mice (n=15). Original magnification: 200X. (C) Representative lung sections and quantification of lung metastatic area after haematoxylin-eosin staining (H&E) (FIJI software analysis) are shown. The arrows indicate the metastatic areas. Quantifications of the percentage of lung metastases are shown in the graphs

50

1125   below; all tumors *$p<0.05$ *vs.* wild-type mice (n=15) and primary tumors with

1126   similar size, *$p<0.01$ *vs.* wild-type mice (n=3). Original magnification: 10X.